Journal of Applied Physics

RESEARCH ARTICLE | OCTOBER 08 2026

Device-scale modeling of valley photovoltaics

Daixi Xia ; Hassan Allami ; Jacob J. Krich

Check for updates

J. Appl. Phys. 140, 143102 (2026)
https://doi.org/10.1063/5.0345370

View Online Export Citation

Articles You May Be Interested In

On-chip terahertz tunable topological valley photonic crystals

J. Appl. Phys. (July 2025)

Spin–valley splitting and spontaneous valley polarization in antiferromagnetic $Mn_2P_2X_3Y_3$ monolayers

Appl. Phys. Lett. (June 2023)

Spin-valley coupling and valley splitting in the $MoSi_2N_4/CrCl_3$ van der Waals heterostructure

Appl. Phys. Lett. (November 2021)

08 October 2026 14:11:18

AIP Publishing

Journal of Applied Physics ARTICLE pubs.aip.org/aip/jap

Device-scale modeling of valley photovoltaics

Cite as: J. Appl. Phys. **140**, 143102 (2026); doi: 10.1063/5.0345370
Submitted: 26 May 2026 · Accepted: 18 September 2026 ·
Published Online: 8 October 2026

View Online Export Citation CrossMark

Daixi Xia,[1,a)] Hassan Allami,[1] and Jacob J. Krich[1,2]

AFFILIATIONS

[1]Department of Physics, University of Ottawa, Ottawa, Canada
[2]Nexus for Quantum Technologies, University of Ottawa, Ottawa, Canada

[a)]**Author to whom correspondence should be addressed:** dxia031@uottawa.ca

ABSTRACT

We present a Poisson/drift-diffusion model that includes valley scattering effects for simulating valley photovoltaic devices. The valley photovoltaic concept is a novel implementation of a hot-carrier solar cell and leverages the valley scattering effect under large electric field to potentially achieve high voltage and high efficiency. Fabricated devices have shown S-shaped current–voltage curves, low fill factor, and, thus, low efficiency. We hence develop the first device model for valley photovoltaics. Our model includes quasi-equilibrated carrier populations in the satellite valleys and electric-field-dependent valley scattering rates extracted from previous ensemble Monte Carlo simulations. We show that nonequilibrium carrier populations in the valleys are not enough for valley photovoltaics to achieve high efficiency. Within our model, we also show that increasing the built-in electric field in the valley-scattering region does not improve efficiency, contrary to previous suggestion. Since our model does not show high efficiencies, achieving high efficiency valley photovoltaics requires producing high carrier temperatures—in addition to the separated carrier populations included in our model—or architecture changes from the existing devices.

Published under an exclusive license by AIP Publishing. https://doi.org/10.1063/5.0345370

08 October 2026 14:11:18

I. INTRODUCTION

Hot carrier solar cells have a high maximum theoretical efficiency of 86% under full concentration, significantly higher than the Shockley–Queisser limit.[1] The high theoretical ceiling is achieved by absorbing low-energy photons while reducing thermalization loss in carriers generated by high-energy photons. A hot-carrier cell must (1) sustain non-equilibrium carrier distributions and (2) have energy-selective contacts.[2] The valley photovoltaic (VPV) is a new concept for hot-carrier cells, illustrated in Fig. 1(a), where carriers produced in the Γ valley in the Brillouin zone of the conduction band scatter to satellite valleys. These metastable valley populations can sustain non-equilibrium electron distributions at a higher energy than the conduction band (CB) minimum. Extracting electrons from these valleys results in potentially high operating voltage. The valleys help simultaneously sustain high carrier energies and provide an energy-selective contact. Reference 3 studied a VPV device sketched in Fig. 1(c) with n^+-$In_{0.52}Al_{0.48}As$, n-$In_{0.53}Ga_{0.47}As$, and p^+-$In_{0.52}Al_{0.48}As$ on an InP substrate. The design has a high built-in electric field in InGaAs that is hypothesized to encourage valley scattering from the Γ valley to the L valley.[3–5] The InAlAs layers are designed to extract electrons from the L valley of InGaAs, as illustrated in Fig. 1(d). The device in Ref. 3 shows distinct S-shaped current–voltage (JV) curves and, therefore, low fill factor and efficiency, as shown in Fig. 2. Reference 5 suggested that a thinner InGaAs layer, hence larger built-in field, produces more carriers in L through valley scattering (VS). Current theoretical studies of VPV have used ensemble Monte Carlo (EMC) calculations in homogenous InGaAs medium without the InAlAs layers and device details.[4] To explain VPV devices, we need a computationally efficient device model.

In this work, we develop a Poisson/drift-diffusion (PDD) model, with separate populations in the Γ and L valleys, each separately quasi-thermalized at lattice temperature. We include valley scattering as recombination and generation between Γ and L populations and use rates extracted from EMC results provided by David Ferry through private communications, through calculations performed similarly to those in Ref. 4. We incorporate those rates into the PDD model by introducing a quasi-electric field that enables agreement with both EMC rates when carrier concentrations are homogeneous and detailed balance at thermal equilibrium. In our model, we include no genuine hot-carrier effect, as all carriers are thermalized to the lattice temperature, but we consider carrier distributions that are highly non-quasi-equilibrium when compared with a standard two-band model of a

Published under an exclusive license by AIP Publishing

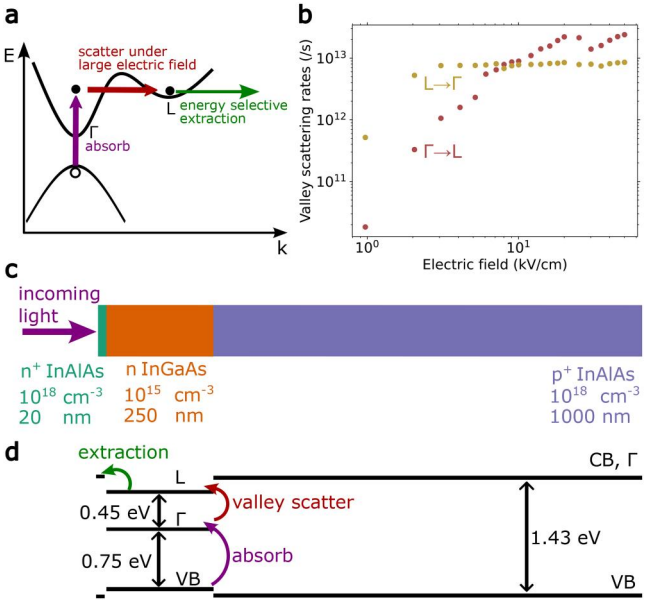

FIG. 1. (a) Schematic of the InGaAs band structure. VPV devices are designed to facilitate net valley scattering from Γ to L valleys and aim to extract from L valleys. (b) Valley scattering rates extracted from EMC results.[4] Γ-to-L rate exceeds L-to-Γ at electric field larger than 10 kV/cm. VPV device design (c) and band-energy alignments (d) from Ref. 3.

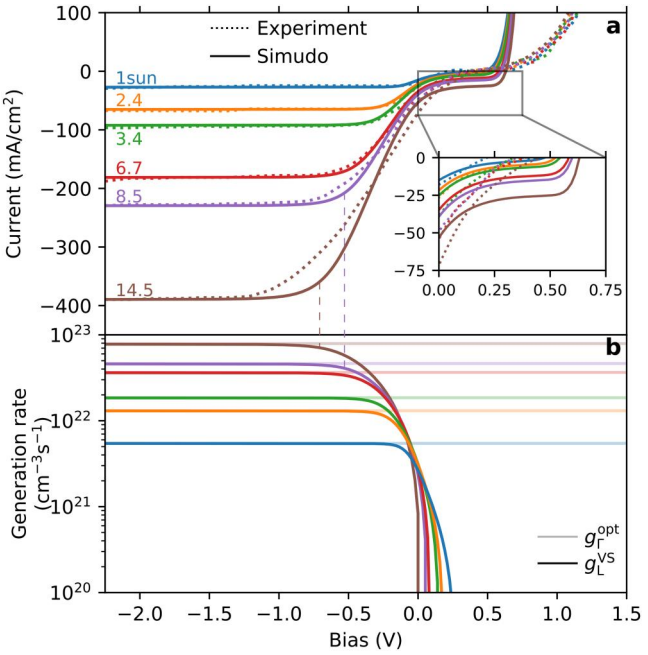

FIG. 2. (a) Current–voltage curves, simulated (solid) and digitized from Ref. 3 (dotted). The simulated currents are all multiplied by 1.09 to match the experimental reverse saturation current at 14.5 suns. (b) Volume averaged valley scattering generation rate to the L valley as a function of voltage for the same illumination levels as in (a); the faded horizontal lines indicate the volume averaged optical generation in the Γ valley. The vertical dashed lines show that the knees of the $J(V)$ curves correspond to the voltages where the VS generation begins to fall below the optical generation. In reverse bias, the device valley scatters to L all optically generated electrons in Γ.

semiconductor. We include the metastability of the carriers in the satellite valleys as well as extraction from these valleys. Our PDD model can qualitatively reproduce the experimental JV curves, including the S shapes, even in the absence of nonradiative recombination processes. While S-shaped $J(V)$ curves are normally associated with extraction barriers,[6] our simulation results show that the valley scattering process can also cause S shapes. With our model, we study the effect of built-in electric field by varying the thickness of the InGaAs region. We find that increasing built-in electric field increases valley scattering from Γ to L in reverse bias but does not help with efficiency in the forward bias where the device produces energy. Our model assumes that the hot CB carriers produced by valley scattering can be described with separated Γ and L valley populations that are each quasi-equilibrated with the lattice. Any future efficient VPV devices must violate this assumption or use a different device architecture.

II. VALLEY SCATTERING EFFECT AND EXISTING MODELS

Valley scattering is a type of electronic intraband transition caused by phonon scattering that moves electrons between regions of the Brillouin zone. The phonon momentum matches the momentum difference between the initial and final valleys. By energy conservation, the energies of the initial and final electronic states differ by the phonon energy. With strong optical generation and valley scattering, the Fermi distribution is not sufficient to describe the CB population, even with an elevated carrier temperature.[4]

One can include valley scattering in some transport models, such as the non-equilibrium Green's function (NEGF) formalism[7] and models based on solving the Boltzmann transport equation (BTE).[4,8–11] The NEGF formalism has an advantage in simulating nanostructures but can be computationally expensive for micrometer-scale devices.[7] BTE solves the semiclassical electron dynamics and can be directly computed with EMC.[8] EMC determines the energetic distribution of electrons and does not assume a form for that distribution. Reference 4 studied the valley scattering effect for photovoltaic purposes using an EMC model in a homogeneous medium. The EMC formalism can include device transport. However, a device EMC model requires larger computational resources than in a homogeneous medium,[8] so EMC models are generally used for thin devices or in a hybrid model where EMC is applied in a small portion of the device.[12,13]

The BTE can also be computed indirectly by expanding in moments of the population distribution.[11] The infinite moment equations are truncated, and a closure relation is asserted. PDD equations are the zeroth- and first-moment equations of the BTE, where the electron distribution function is Fermi–Dirac, while

08 October 2026 14:11:18

Published under an exclusive license by AIP Publishing

hydrodynamic (HD) models include a small number of higher moments. The HD models were designed to study Gunn oscillators and were also used for metal-oxide-semiconductor field-effect transistors (MOSFETs) in the early 2000s. The HD models allow for simulating energy transport independent of particle transport, allowing prediction of varying carrier temperature.[9,10] In the PDD case, the carrier population is determined completely by the quasi-Fermi level, and the carrier temperature is equal to the lattice temperature. We choose the PDD model for simulating valley photovoltaics because it is computationally efficient when including optical absorption and device transport, allows for a simple implementation of valley scattering (detailed in Sec. III), and is standard in photovoltaic calculations.

III. PDD MODELING OF VALLEY SCATTERING

We develop a multi-band PDD model that includes both optical absorption and valley scattering. We model valley scattering in a multi-band PDD framework, using Simudo, which is a finite-element-based PDD device model capable of simulating multiple bands with transport.[14] We treat the Γ and the L valleys as separate bands, each with its own carrier population with separate quasi-Fermi levels.

In PDD, the carrier concentration u_k in a band k is related to the current density $\boldsymbol{j}_k$ in that band by the drift-diffusion and continuity equations,

$$\begin{aligned} \boldsymbol{j}_k &= q\mu_k u_k \nabla w_k, \\ \frac{\partial u_k}{\partial t} &= -s_k \frac{1}{q} \nabla \cdot \boldsymbol{j}_k + g_k^{\text{net}}, \end{aligned} \tag{1}$$

where $s_k = -1$ for negative-charge carriers in a conduction band, including Γ and L valleys, $s_k = +1$ for holes in the valence band, μ_k is the carrier mobility, w_k is the quasi-Fermi energy, and q is the elementary charge. Equation (1) contains both drift and diffusion terms and is valid for carrier populations obeying Boltzmann and Fermi statistics.[15] g_k^{net} is the net generation to band k due to absorption and recombination processes and can be separated into several terms, each representing a different process,

$$g_k^{\text{net}} = g_k^{\text{opt}} + g_k^{\text{rad}} + g_k^{\text{non-rad}} + g_k^{\text{VS}}, \tag{2}$$

where g_k^{opt} is the optical generation, g_k^{rad} is the net radiative recombination, and $g_k^{\text{non-rad}}$ is the non-radiative recombination, such as Shockley–Read–Hall and Auger processes. Those g_k terms are standard in PDD device models. g_k^{VS} is the net generation due to the valley-scattering process. Incorporating g_k^{VS} into PDD modeling is the focus of this study. In steady state, $\frac{\partial u_k}{\partial t} = 0$. The carrier distribution must also obey Poisson's equation,

$$\nabla \cdot (\epsilon \nabla \phi) = -\rho, \tag{3}$$

where ϵ is the permittivity, ϕ is the electrostatic potential, and ρ is the charge density.

We assume parabolic dispersion for all bands, which gives the standard connection between the quasi-Fermi levels w_k and the carrier concentrations,

$$u_k = \begin{cases} \frac{1}{2\pi^2}\left(\frac{2m_k^*}{\hbar^2}\right)^{3/2} \int_{E_k}^{\infty} \frac{(E-E_k)^{1/2} \mathrm{d}E}{e^{(E-w_k-q\phi)/k_\mathrm{B}T}+1}, & \text{CB}, \\ \frac{1}{2\pi^2}\left(\frac{2m_k^*}{\hbar^2}\right)^{3/2} \int_{-\infty}^{E_k} \frac{(E_k-E)^{1/2} \mathrm{d}E}{e^{-(E-w_k-q\phi)/k_\mathrm{B}T}+1}, & \text{VB}, \end{cases} \tag{4}$$

where $\hbar$ is the reduced Planck's constant, m_k^* is the effective mass, E_k is the band extremum, ϕ is the electrostatic potential, k_B is the Boltzmann constant, and $T = 300\,\mathrm{K}$ is the temperature. In bands where $s_k(w_k + q\phi - E_k) \gg k_\mathrm{B}T$, Eq. (4) reduces to the standard Boltzmann result,

$$u_k = N_k e^{s_k(E_k - w_k - q\phi)/k_\mathrm{B}T}, \tag{5}$$

where $N_k = 2\left(\frac{m_k^* k_\mathrm{B} T}{2\pi\hbar^2}\right)^{3/2}$ is the effective density of states. For degenerate bands where we cannot take the Boltzmann approximation, numerically calculating $u_k(w_k)$ and the inverse, $w_k(u_k)$, is slow due to the Fermi integral. We use the Joyce and Dixon approximation for parabolic bands, which uses Lambert W function defined as $W(z)e^{W(z)} = z$.[16] Then, the population can be approximated as

$$u_k = \frac{N_k}{A_1} W\left[A_1 e^{s_k(E_k - w_k - q\phi)/k_\mathrm{B}T}\right], \tag{6}$$

where $A_1 = 2^{-3/2}$. The closed-form inverse function is $w_k(u_k) = E_k - q\phi - s_k k_B T[\ln(u_k/N_k) + A_1 u_k/N_k]$.

We use a static absorption profile g_k^{opt} with more details described in Sec. IV. Radiative recombination rates g_k^{rad} are given by the van Roosbroeck–Shockley relation.[17] Standard Shockley–Read–Hall (SRH) and Auger recombinations are also included in the $g_k^{\text{non-rad}}$ term. More details on Simudo can be seen in Ref. 14. In this work, we only present results with $g_k^{\text{non-rad}} = 0$, because that is sufficient to capture the major qualitative features of the existing candidate VPV devices.

We express valley scattering as generation and recombination in the Γ and L valleys, with electric-field-dependent rates r_k extracted from the EMC results in Fig. 1(b). The total valley scattering rate is dependent on the populations in each valley,

$$g_\mathrm{L}^{\text{VS}} = r_\Gamma u_\Gamma - r_\mathrm{L} u_\mathrm{L}, \tag{7}$$

where u_Γ and u_L are the carrier concentrations in the Γ and L valleys, respectively. In equilibrium, $g_\mathrm{L}^{\text{VS}} = 0$.

Interpreting the EMC VS rates of Fig. 1(b) naively would present a contradiction at equilibrium. Specifically, for the device shown in Fig. 1(c), the built-in electric field in the InGaAs region is ≃25 kV/cm at equilibrium. The EMC results in Fig. 1(b) show that $r_\Gamma > r_\mathrm{L}$ at 25 kV/cm. Since detailed balance requires that at equilibrium, $g_\mathrm{L}^{\text{VS}} = 0$, we would conclude that $\frac{u_\mathrm{L}^{\text{eq}}}{u_\Gamma^{\text{eq}}} > 1$. Here, u_k^{eq} is the carrier population in band k at equilibrium and is obtained by setting $w_k = w^{\text{eq}}$ in Eq. (5) or (6). However, in equilibrium, carrier populations of the valleys are decided by the valley energy levels

08 October 2026 14:11:18

Published under an exclusive license by AIP Publishing

and the equilibrium Fermi level, which is the same for both valleys' populations, so, in reality, $\frac{u_L^{eq}}{u_\Gamma^{eq}} \ll 1$. This contradiction arises because the EMC simulations are performed in a spatially invariant sample. To resolve this apparent contradiction, we introduce the quasi-electric field of a valley k as

$$\mathcal{E}_k = \frac{\nabla w_k}{q}. \tag{8}$$

This replacement of the physical electric field with the gradient of a quasi-Fermi level is similar to the well-known formulation of band currents as $j_k = q\mu_k u_k \nabla w_k$, which expresses drift and diffusion properties as a drift current with respect to the quasi-electric field.[18] In the uniform-medium limit, the quasi-electric field is the physical field: $\mathcal{E}_k = \nabla w_k/q = -\nabla\phi$. We can derive this relation by noting that in uniform medium, carrier concentration is constant, so from Eqs. (5) and (6), $\nabla[s_k(E_k - w_k - q\phi)/k_B T] = 0$, so in a uniform material, $\nabla E_k = 0$ and $\nabla w_k = -q\nabla\phi$. Therefore, our definition of $\mathcal{E}_k$ is consistent with the uniform-medium EMC simulations.[4] At equilibrium, $\mathcal{E}_k = 0$, which correctly gives $g_L^{VS} = 0$. We reinterpret the abscissa of Fig. 1(b) as being $\mathcal{E}$ for each valley. Then, $r_\Gamma = r_\Gamma(\mathcal{E}_\Gamma)$ and $r_L = r_L(\mathcal{E}_L)$. We, thus, incorporate valley scattering into the model, obeying both the EMC limit and the carrier distribution at equilibrium. Unlike in EMC simulations, we do not include the non-quasi-equilibrium carrier distribution or elevated carrier temperature possible in real devices. In the steady-state limit, the return to a Fermi–Dirac distribution is reasonable, but the temperature is a bigger approximation. Reference 3 reports measurements of the high-energy photoluminescence tail, which indicate elevated carrier temperatures in the Γ valley. A hydrodynamic model would be required to treat separate carrier temperatures in each valley.[10]

The EMC data in Fig. 1(b) do not have data at equilibrium, $\mathcal{E} = 0$. Under the equilibrium condition, we know that $g_L^{VS} = 0$, so we have only one unknown equilibrium rate, since setting $r_L(0)$ determines $r_\Gamma(0)$. In principle, $r_L(0)$ is a calculable physical quantity, but we do not currently have access to its value. We take $r_L(0)$ as a tunable parameter. There are many ways to connect the equilibrium scattering rates to the EMC data at finite $\mathcal{E}$. We find that linear interpolation gives rise to numerical instability. The lowest few r_L and r_Γ EMC points show a roughly quartic increase with $\mathcal{E}$. Therefore, we opt to connect the equilibrium rates and the lowest EMC data points with two-parameter quartic functions,

$$r_k(\mathcal{E}_k) = a(\mathcal{E}_k - b)^4, \tag{9}$$

where the parameters a and b are determined by $r_k(0)$ and the EMC data point with the lowest $\mathcal{E}$.

The low-field extrapolation of r_Γ and r_L needs to obey equilibrium detailed balance in a device: $g_L^{VS}(\mathcal{E}_k = 0, w_k = w^{eq}) = 0$. We can satisfy this condition by setting $r_L(0)/r_\Gamma(0) = u_\Gamma(w^{eq})/u_L(w^{eq})$. In this work, the Γ valley carriers obey Fermi statistics, Eq. (4), so the w^{eq} dependence is not eliminated in the ratio $u_\Gamma(w^{eq})/u_L(w^{eq})$. Then, the equilibrium relation between $r_L(0)$ and $r_\Gamma(0)$ depends on w^{eq},

$$r_\Gamma(\mathcal{E}_\Gamma = 0, w^{eq}) = r_L(0)\frac{u_L(w^{eq})}{u_\Gamma(w^{eq})}. \tag{10}$$

At zero field but out of equilibrium, it is unphysical for $r_\Gamma(\mathcal{E}_\Gamma = 0)$ to still depend on w^{eq}. Therefore, in Eq. (10), we use w_Γ in place of w^{eq}. In our low-field approximation, r_Γ depends on both $\mathcal{E}_\Gamma$ and w_Γ.

An ideal VPV device has large g_L^{VS}, so the device generally benefits from large r_Γ and small r_L. From Fig. 1(b), r_Γ increases as $\mathcal{E}_\Gamma$ increases until $\mathcal{E}_\Gamma$ reaches around 20 kV/cm when the increase in r_Γ slows. For achieving small r_L, we would need small $\mathcal{E}_L$, although r_L is not sensitive to $\mathcal{E}_L$ when it exceeds 3 kV/cm.

IV. SIMULATING A VALLEY PHOTOVOLTAIC DEVICE

We study the structure shown in Fig. 1(c), with thicknesses and dopings as indicated. Table I lists physical parameters used in our simulations. We use a static Beer–Lambert optical generation profile for each band, $g_k^{opt}(z)$, as a function of depth z into the device. We calculate $g_k^{opt}(z)$ using the AM1.5G spectrum and energy-dependent absorption coefficients.[19,20] Here, we assume the InGaAs VB-to-L absorption is 1% of the VB-to-CB absorption for the energies where it is energetically allowed. In InGaAs, VB-to-L absorption is indirect, which is assumed to be small compared to the direct VB-to-Γ absorption. Radiative recombination rates are calculated according to the van Roosbroeck–Shockley relation.[17] All other material parameters are taken from Ref. 21.

We simulate two carrier populations, in the valence and conduction bands, in the InAlAs regions and three populations in the InGaAs region, where Γ and L valley populations are separate. In our model, we use a thermionic boundary condition between the L valley of the InGaAs region and the CB of InAlAs,[22] and we impose a non-conductive boundary condition for the Γ valley at the heterojunction interfaces. Therefore, carriers in the Γ valley can only be extracted if they first scatter to the L valley. These assumptions are optimistic for the voltage of the device, matching how the devices are proposed to operate and are compatible with achieving high open-circuit voltage V_{oc}. We have also considered carrier extraction directly from the Γ valley; in the

TABLE I. Simulation parameters for $In_{0.52}Al_{0.48}As$ and $In_{0.53}Ga_{0.47}As$ lattice-matched to InP. All material parameters from Ref. 21.

Parameter	Value
$\mu_{L,InGaAs}$	444 $cm^2/V/s$
$\mu_{\Gamma,InGaAs}$	1.39×10^4 $cm^2/V/s$
$\mu_{VB,InGaAs}$	490 $cm^2/V/s$
$\mu_{CB,InAlAs}$	517 $cm^2/V/s$
$\mu_{VB,InAlAs}$	136 $cm^2/V/s$
$N_{\Gamma,InGaAs}$	2.10×10^{17} cm^{-3}
$N_{L,InGaAs}$	6.67×10^{19} cm^{-3}
$N_{VB,InGaAs}$	7.37×10^{18} cm^{-3}
$N_{CB,InAlAs}$	4.85×10^{17} cm^{-3}
$N_{VB,InAlAs}$	1.10×10^{19} cm^{-3}
$E_{\Gamma,InGaAs}$	0.72 eV
$E_{L,InGaAs}$	1.25 eV
$E_{VB,InGaAs}$	0 eV
$E_{CB,InAlAs}$	1.31 eV
$E_{VB,InAlAs}$	−0.14 eV

08 October 2026 14:11:18

Published under an exclusive license by AIP Publishing

supplementary material, Fig. S1c shows simulated $J(V)$ curves of the Γ-extraction scenario, which also show the S shape. In all simulations, we use Fermi statistics for the carriers in the Γ valley, while other bands have Boltzmann statistics. The Γ valley becomes highly degenerate close to the front heterojunction, while other bands stay nondegenerate in the injection levels relevant to this study.

Our model qualitatively reproduces important features of the experimental $J(V)$ curves from Ref. 3: reverse saturation currents with varying illumination intensity, S-shaped $J(V)$ curves, and the shift of the knee in the S shape to more negative bias voltage with increased illumination. Figure 2(a) shows the $J(V)$ curves from the experiment and our simulations. We observe in our simulations that the value of $r_L(0)$ determines the amount of S shape in the $J(V)$ curves. In this work, we choose $r_L(0) = 2 \times 10^7\ s^{-1}$, which best matches the knee in the S shape. The reverse saturation currents are determined by optical absorption. Our model underestimates the reverse saturation currents by about 10%. We adjust all our simulated currents by a single factor of 1.09, such that our reverse saturation current at 14.5 suns matches the experiment. With this one adjustment factor, simulated currents at other intensities match well with the experiments. As shown in the inset of Fig. 2(a), in the power-generating quadrant, the simulations show plateaus at negative current just below V_{oc} and overestimate V_{oc}. This current and voltage overestimate is due to our model overestimating the absorption in the top InAlAs layer. We have simulated versions (Fig. S2 in the supplementary material) without optical absorption in the top InAlAs, in which case our model shows plateaus near $J = 0$, as in the experiment. Our simulations use the nominal thicknesses of the device layers; if the as-grown devices had thinner top InAlAs layers than designed, the agreement with our simulations would be strong. In forward bias, our model predicts a smaller ideality factor than the experimental data, which has an ideality factor of close to 10 (Fig. S2 in the supplementary material). The large ideality factor may be attributed to a non-Ohmic shunt.[23,24] In the supplementary material, we add an external shunt diode and series resistance and fit the associated parameters to the experimental $J(V)$. The fitted $J(V)$ curves show good agreement in the large-forward bias region while still showing S-shape $J(V)$ curves where the knee shifts to more negative voltage with increased illumination.

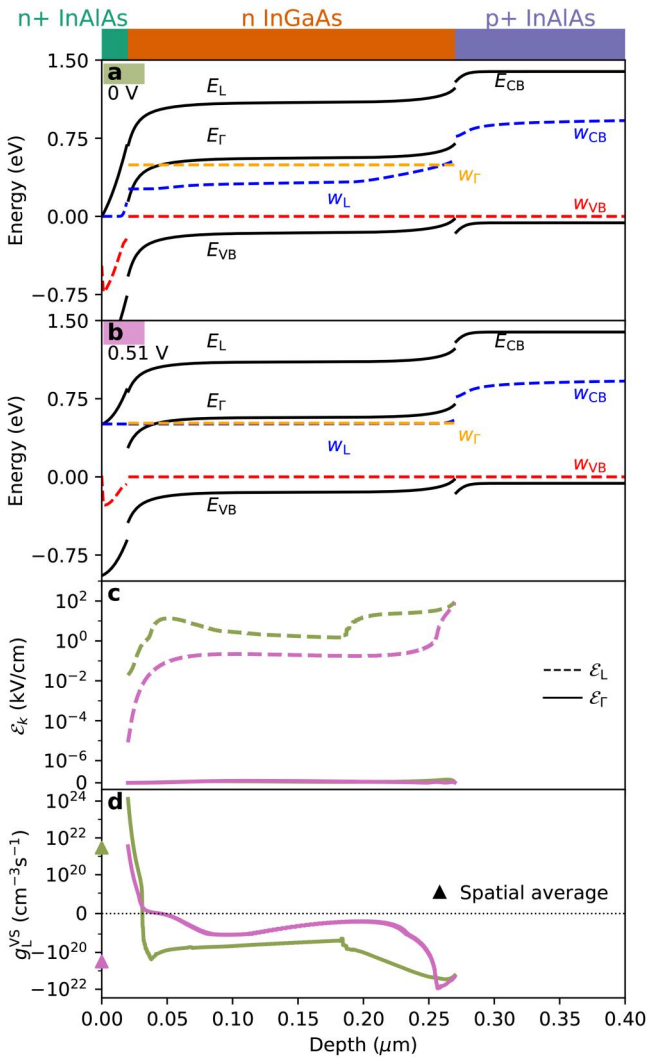

FIG. 3. Simulated with one-sun illumination, $r_L(0) = 2 \times 10^7$/s. Band diagrams at (a) short circuit and (b) 0.51 V. (c) Quasi-electric field as a function of depth of the device in the L (dashed) and Γ (solid) valleys at short circuit and 0.51 V. Colors correspond to the voltages in (a) and (b). (d) Valley scattering generation to L as a function of depth of the device. The triangles indicate the spatial average.

We show in Fig. 2(b) that the S shape in the $J(V)$ curves is caused by the reduction of g_L^{VS} when the voltage increases. In reverse bias, all optically generated electrons in the Γ valley are scattered to L and hence can be extracted. However, as the voltage increases, g_L^{VS} decreases and eventually becomes negative. When $g_L^{VS} < 0$, the electrons are scattered from L to Γ, opposite to what is desired in a high-efficiency VPV. The shoulders of g_L^{VS} in Fig. 2(b), where VS begins to decline, match the onset of the S-shape in Fig. 2(a), demonstrated by the vertical dashed lines, with onset at lower V with higher intensity.

We can understand why g_L^{VS} decreases with voltage by looking at band diagrams. Figures 3(a) and 3(b) show band diagrams under one sun at short circuit and 0.51 V. At short circuit, the majority of the optically generated electrons are scattered to L, while at 0.51 V, there is net transfer from L back to Γ, reducing total current. From Eq. (7), g_L^{VS} depends on both $\mathcal{E}_k$ and u_k. We now take a closer look at the spatially dependent $\mathcal{E}_k$. The band diagrams in Figs. 3(a) and 3(b) show that w_Γ is flat in both voltages, corresponding to near-zero $\mathcal{E}_\Gamma$, plotted in Fig. 3(c). At short circuit, $\mathcal{E}_L$ is approximately 10 kV/cm in a large part of the InGaAs region and is close to 100 kV/cm at the bottom. The resulting quasi-electric field serves to increase the undesirable L-to-Γ scattering. At 0.51 V, $\mathcal{E}_L$ is smaller than 1 kV/cm except toward the bottom, where $\mathcal{E}_L$ has a similar value to the short-circuit case. Now, we move our examination from $\mathcal{E}_k$ to u_k. As seen in the band diagrams in Figs. 3(a) and 3(b), the populations

08 October 2026 14:11:18

Published under an exclusive license by AIP Publishing

are largest at the front of the InGaAs region due to strong optical absorption at the first 20 nm. In particular, $u_\Gamma > u_L$ because the direct-gap VB-to-Γ transition has a much larger absorption coefficient. Therefore, despite $\mathcal{E}_L > \mathcal{E}_\Gamma$, the effect of carrier population outweighs the effect of quasi-electric fields. As shown in Fig. 3(d), the resulting g_L^{VS} is then largest at the front of the InGaAs. In forward bias, at 0.51 V, the front g_L^{VS} is smaller than that at short circuit. Therefore, the volume-total g_L^{VS} at 0.51 V is negative.

Efficient VPV requires achieving a voltage larger than the InGaAs Γ-valley bandgap E_g^Γ, but both experimental and simulated devices have $V_{oc} < E_g^\Gamma$. In our model, the small V_{oc} occurs because the net VS generation is dominated by the zero-field VS rates. If we consider w_L to be spatially constant, as is approximately true in forward bias [Fig. 3(b)], then V_{oc} is limited by $w_L - w_{VB}$, with w_{VB} evaluated at the p-type contact, at the back of the device. When $\mathcal{E}_k \ll 1$ kV/cm, from Eqs. (7) and (10), the net scattering rate is

$$g_L^{VS}(\mathcal{E}_\Gamma, \mathcal{E}_L = 0) = u_L r_L(0)\left[\exp\left(\frac{w_\Gamma - w_L}{k_B T}\right) - 1\right]. \quad (11)$$

We include a derivation of Eq. (11) in the supplementary material. From this form, we can see that g_L^{VS} is negative when $w_L > w_\Gamma$. Therefore, to efficiently scatter Γ valley electrons to L, w_L needs to be less than w_Γ. Since radiative recombination forces $w_\Gamma - w_{VB} < E_g^\Gamma$, if there is positive current from Γ to L, then $w_L - w_{VB} < w_\Gamma - w_{VB} < E_g^\Gamma$. Therefore, the device's V_{oc}, bounded by $w_L - w_{VB}$, cannot exceed E_g^Γ. This constraint rules out the possibility of high-efficiency VPV devices, which must be able to obtain higher voltages.

The above simulations agree with the experimental results that the studied InGaAs VPV device does not produce high efficiency. We now consider what happens to VS efficiency if we allow the material properties to change, as in a hypothetical material with stronger VS processes. In Sec. VI, we return to InGaAs and consider the effects of changing the thickness—and, thus, the equilibrium electric field—of the InGaAs region.

V. EFFECTS OF EQUILIBRIUM VALLEY SCATTERING RATES ON S SHAPE $J(V)$

We consider a range of hypothetical materials by considering the effects of changing $r_L(0)$ and show that the S shape in $J(V)$ can be eliminated by increasing $r_L(0)$, but V_{oc} is still limited by the InGaAs bandgap. Figure 4(a) shows the one-sun $J(V)$ curves simulated for the same device structure shown in Fig. 1(c). Smaller $r_L(0)$ values result in smaller fill factors, i.e., more "S" shaped $J(V)$. For $r_L(0) \gtrsim 10^9$ s^{-1}, $J(V)$ becomes diode like. Although larger $r_L(0)$ increases fill factor, V_{oc} decreases asymptotically to ≃0.52 V.

The S-shaped JV and low fill factor are due to insufficient net valley scattering from the Γ to the L valley. Figure 4(b) shows volume-averaged g_L^{VS} as a function of voltage. In reverse bias, valley scattering can bring all optically generated electrons in Γ to L for all $r_L(0)$ values except the lowest case, but the net VS generation rate

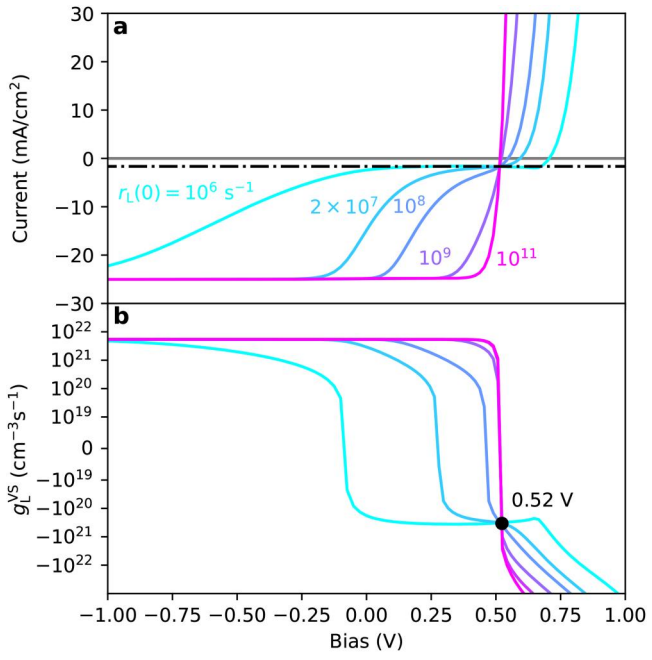

FIG. 4. (a) One-sun $J(V)$ curves simulated with different values of $r_L(0)$. The $J(V)$ matches experiments the best with $r_L(0) = 2 \times 10^7$ s^{-1}. The dotted-dashed line is the photocurrent in the top InAlAs region. (b) Spatially averaged g_L^{VS} as a function of voltage for various $r_L(0)$ values.

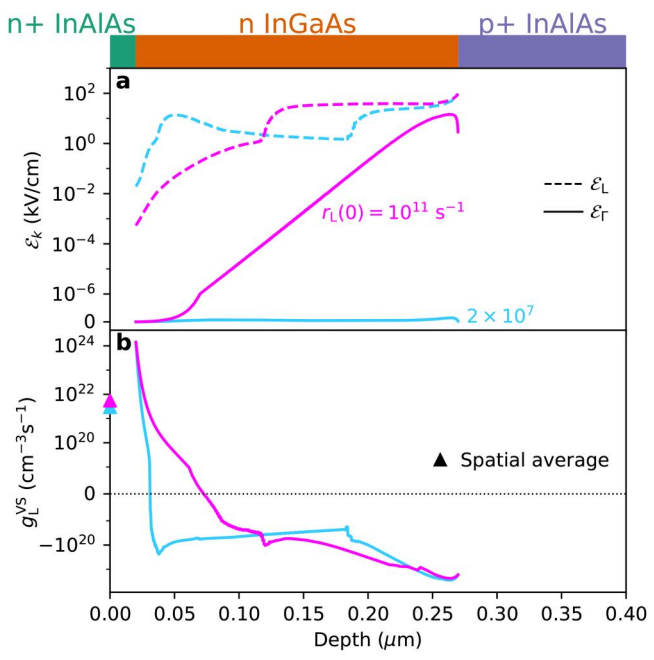

FIG. 5. Under one-sun illumination, 0 V, (a) $\mathcal{E}_k$ and (b) g_L^{VS} as a function of device depth for the two choices of $r_L(0)$ in Fig. 4. $r_L(0) = 2 \times 10^7$ s^{-1} gives the best match of $J(V)$ to experiments. The volume averaged $g^0_{\Gamma\to L}$ are indicated as triangles on the y axis.

08 October 2026 14:11:18

Published under an exclusive license by AIP Publishing

decreases as the voltage increases. With larger $r_L(0)$, VS generation decreases more slowly as the voltage becomes positive. However, the trend reverses as V approaches 0.52 V, where larger $r_L(0)$ results in more negative VS generation, opposing photocurrent.

Under our model, for a VPV device to achieve high efficiency, we need to have a large $\mathcal{E}_\Gamma$, which could permit g_L^{VS} to be larger while still having $w_L > w_\Gamma$, which would enable increased V_{oc}. In Fig. 5(a), $\mathcal{E}_\Gamma$ becomes large near the bottom of the InGaAs region for $r_L(0) = 10^{11}\ s^{-1}$. Figure 5(b), which plots the net VS generation to L, shows that despite this large $\mathcal{E}_\Gamma$, g_L^{VS} is still small at the bottom, since the u_Γ in this region is small. Hence, the advantage of large $\mathcal{E}_\Gamma$ does not show in the net current. Future designs of VPV can focus on creating large $\mathcal{E}_\Gamma$ on the top portion of InGaAs, where u_Γ is large.

VI. LARGE BUILT-IN FIELD DOES NOT IMPROVE EFFICIENCY

Reference 5 proposed that a thinner InGaAs region, hence with larger built-in electric field, results in more valley scattering to L, which is beneficial to VPV devices. In this section, we test this hypothesis with our model and show that larger built-in field does not facilitate more generation to L through valley scattering in forward bias and, therefore, does not improve efficiency.

In our simulations, we vary the thickness of InGaAs from 10 to 250 nm. The structures with thinner InGaAs regions have larger built-in fields than those with thicker InGaAs. Figure 6(a) shows increasing fill factor with thinner InGaAs despite reduced reverse saturation currents as the InGaAs absorber becomes thin. The increased fill factor is consistent with that reported in Ref. 5. Our model shows that the cause of this phenomenon is not as proposed in Ref. 5.

The increased fill factor comes solely from the increased absorption in the bottom InAlAs region due to higher transparency as the InGaAs layer is made thinner. Figure 6(b) shows g_L^{VS} and g_L^{opt}, averaged over volume. In structures with thinner InGaAs, the net valley scattering rate is larger in reverse bias due to larger per-volume optical absorption. We plot g_L^{VS} and g_L^{opt} as functions of voltage in Fig. 6(b). In the reverse saturation region, $g_L^{VS} = g_L^{opt}$ for the devices of all InGaAs layer thickness. Independent of the built-in electric-field strength, every structure scatters to L all electrons that are optically generated at Γ. However, g_L^{VS} decreases rapidly around $V = 0$. In forward bias, near maximum power point (mpp), $g_L^{VS} < 0$ for all structures, hurting the overall current. Although the thinnest InGaAs has larger V_{oc} and larger current at mpp as shown in Fig. 6(a), the thinnest InGaAs actually has its forward-bias current most strongly reduced by valley scattering. In Fig. 6(b), g_L^{VS} is more negative with thinner InGaAs. In the thinnest case with 10 nm InGaAs, around 0.6 V, the device has a nonmonotonic $J(V)$ and g_L^{VS}. However, g_L^{VS} is still negative when the current magnitude increases, so the current and the efficiency are still hurt by valley scattering in forward bias. Eliminating the InGaAs layer altogether results in the largest fill factor, largest V_{oc}, and highest efficiency, as shown with the red $J(V)$ curve in Fig. 6(a).

To see the cause for the increased fill factor with thinner InGaAs, we plot g_L^{net} in the InGaAs region, including valley scattering, optical generation, and radiative recombination, as dashed lines in Fig. 6(c). The solid lines in Fig. 6(c) are sums of g_L^{net} in InGaAs and g_{CB}^{net} in InAlAs. The difference between the solid and the dashed lines is the optical generation, net of radiative recombination, in the InAlAs regions. With thinner InGaAs, more light reaches the bottom InAlAs layer. We see that the optical generation in the bottom InAlAs explains the phenomenon where thinner InGaAs region increases current and fill factor.

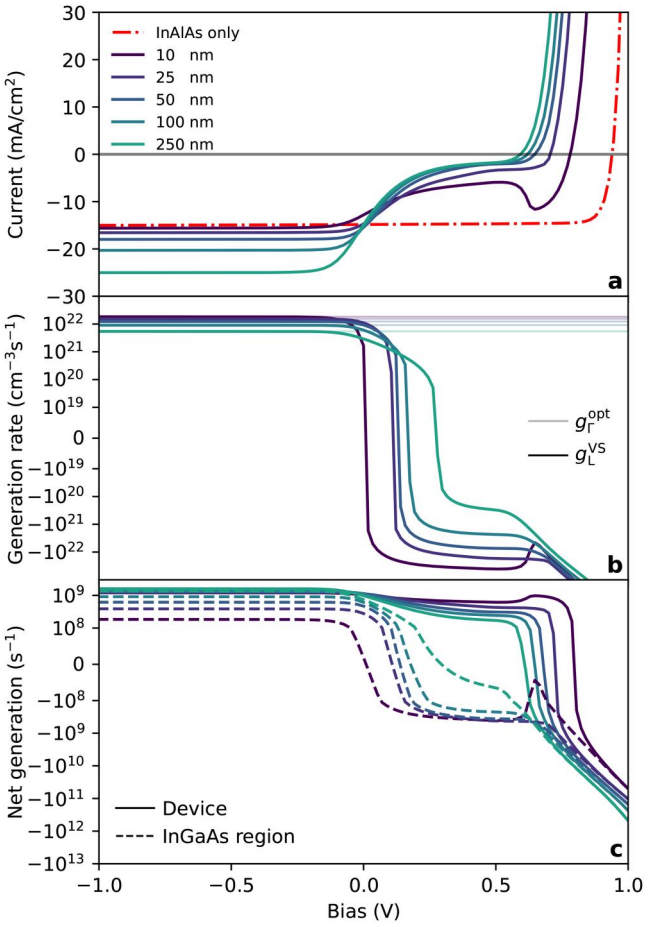

FIG. 6. (a) Current–voltage curves at one sun, with various InGaAs layer thicknesses and for a reference device without InGaAs; (b) volume integrated g_L^{VS} and g_L^{opt}; and (c) net generation to InAlAs CB and InGaAs L valley from optical and valley scattering in all regions (solid) and in the InGaAs layer only (dashed).

VII. DISCUSSION

We have performed device-level simulations of proposed VPV devices using a PDD model. These simulations include quasi-equilibrium carriers in each of the bands so do not include genuine hot-carrier effects beyond quasi-equilibrium. We nonetheless find compelling qualitative agreement with experimental $J(V)$ curves. Within this model, it does not appear that VPV devices can achieve high efficiency. The large reverse-saturation

08 October 2026 14:11:18

Published under an exclusive license by AIP Publishing

current is consistent with the small Γ bandgap in InGaAs, which allows the device to absorb a larger portion of the solar spectrum than the larger-bandgap InAlAs. In principle, if it could maintain separated quasi-Fermi levels of Γ and L while extracting only from L, the device's voltage would be capable of exceeding the small Γ bandgap. We can draw a loose analogy between VPV and intermediate-band solar cells (IBSCs), where Γ valley corresponds to intermediate band and L valley corresponds to IBSC's CB. In IBSC, an electron in IB absorbs a photon and transfers to the CB, while in VPV, an electron in the Γ valley scatters to L. In an intermediate-band solar cell (IBSC), the separated quasi-Fermi levels of the intermediate band (IB) and CB allow for a large voltage that is limited by CB–VB bandgap while at the same time leveraging the IB for absorbing sub-gap photons and increasing photocurrent. Unlike in IBSC, we only observe the increased photocurrent due to VS in reverse bias, and in forward bias, the VS process limits the voltage to the Γ bandgap, instead of the larger L gap. Our model does not include carrier-temperature effects. Deviations from the predictions of our model could be used to prove the existence of non-quasi-equilibrium effects in experiments and whether high efficiencies are possible. Our results show that a high-efficiency VPV device must have not only nonequilibrium populations in the satellite valleys, but there must also be elevated carrier temperatures. This conclusion agrees with the original VPV proposal, though if hot carriers in the satellite valleys are essential to device operation, VPV will require energy-selective contacts similarly to other hot carrier solar cell concepts. Future high-efficiency VPV devices that benefit from the hot-carrier effects will need device modeling beyond drift diffusion that includes varying carrier temperatures, but many features of existing electrical measurements are explainable without contribution from any such high-carrier-temperature populations.

SUPPLEMENTARY MATERIAL

We include supplementary material that contains additional simulation results and a derivation of Eq. (11).

ACKNOWLEDGMENTS

We thank Dave Ferry for sharing the ensemble Monte Carlo valley scattering rates and thank Ian Sellers, Dave Ferry, Ned Ekins-Daukes, and their groups for valuable discussions. We acknowledge NSERC CREATE TOP-SET (Award No. 497981) for funding.

AUTHOR DECLARATIONS

Conflict of Interest

The authors have no conflicts to disclose.

Author Contributions

Daixi Xia: Data curation (equal); Formal analysis (equal); Investigation (equal); Methodology (equal); Software (equal); Validation (equal); Visualization (equal); Writing – original draft (equal); Writing – review & editing (equal). **Hassan Allami:** Formal analysis (equal); Investigation (supporting); Methodology (supporting); Writing – review & editing (supporting). **Jacob J. Krich:** Conceptualization (equal); Data curation (equal); Formal analysis (equal); Funding acquisition (equal); Investigation (equal); Methodology (equal); Project administration (equal); Resources (equal); Software (equal); Supervision (equal); Validation (equal); Visualization (equal); Writing – original draft (equal); Writing – review & editing (equal).

DATA AVAILABILITY

The data that support the findings of this study are available from the corresponding author upon reasonable request.

REFERENCES

[1]P. Würfel, A. S. Brown, T. E. Humphrey, and M. A. Green, "Particle conservation in the hot-carrier solar cell," Prog. Photovolt. Res. Appl. **13**, 277–285 (2005).
[2]M. A. Green, *Third Generation Photovoltaics: Advanced Solar Energy Conversion* (Springer, Berlin, 2003).
[3]H. Esmaielpour, K. R. Dorman, D. K. Ferry, T. D. Mishima, M. B. Santos, V. R. Whiteside, and I. R. Sellers, "Exploiting intervalley scattering to harness hot carriers in III–V solar cells," Nat. Energy **5**, 336–343 (2020).
[4]D. K. Ferry, "In search of a true hot carrier solar cell," Semicond. Sci. Technol. **34**, 044001 (2019).
[5]K. R. Dorman, V. R. Whiteside, D. K. Ferry, T. D. Mishima, I. Yusuf, H. Esmaielpour, M. B. Santos, and I. R. Sellers, "Electric field and its effect on hot carriers in InGaAs valley photovoltaic devices," IEEE J. Photovolt. **12**, 1175–1183 (2022).
[6]R. Saive, "S-shaped current–voltage characteristics in solar cells: A review," IEEE J. Photovolt. **9**, 1477–1484 (2019).
[7]U. Aeberhard, "Theory and simulation of quantum photovoltaic devices based on the non-equilibrium Green's function formalism," J. Comput. Electron. **10**, 394–413 (2011).
[8]C. Jacoboni and P. Lugli, *The Monte Carlo Method for Semiconductor Device Simulation;* Computational Microelectronics (Springer, Wien, 1989).
[9]K. Blotekjaer, "Transport equations for electrons in two-valley semiconductors," IEEE Trans. Electron Devices **17**, 38–47 (1970).
[10]A. M. Anile and S. D. Hern, "Two-valley hydrodynamical models for electron transport in gallium arsenide: Simulation of Gunn oscillations," VLSI Design **15**, 681–693 (2002).
[11]G. Mascali and V. Romano, "Hydrodynamical model of charge transport in GaAs based on the maximum entropy principle," Continuum Mech. Thermodyn. **14**, 405–423 (2002).
[12]P. Muralidharan, S. M. Goodnick, and D. Vasileska, "Modeling of transport in carrier-selective contacts in silicon heterojunction solar cells," Prog. Photovolt. Res. Appl. **30**, 490–502 (2022).
[13]I. Baranowski, I. R. Sellers, D. Vasileska, and S. M. Goodnick, "Monte Carlo simulation of ultrafast carrier relaxation in type-II MQW system," J. Photonics Energy **15**, 012505 (2025).
[14]E. C. Dumitrescu, M. M. Wilkins, and J. J. Krich, "Simudo: A device model for intermediate band materials," J. Comput. Electron. **19**, 111–127 (2020).
[15]F. Poupaud and C. Schmeiser, "Charge transport in semiconductors with degeneracy effects," Math. Methods Appl. Sci. **14**, 301–318 (1991).
[16]W. B. Joyce and R. W. Dixon, "Analytic approximations for the Fermi energy of an ideal Fermi gas," Appl. Phys. Lett. **31**, 354–356 (1977).
[17]W. van Roosbroeck and W. Shockley, "Photon-radiative recombination of electrons and holes in germanium," Phys. Rev. **94**, 1558–1560 (1954).
[18]W. Fichtner, D. J. Rose, and R. E. Bank, "Semiconductor device simulation," SIAM J. Sci. Stat. Comput. **4**, 391–415 (1983).

08 October 2026 14:11:18

Published under an exclusive license by AIP Publishing

[19]S. Adachi, *Physical Properties of III-V Semiconductor Compounds: InP, InAs, GaAs, GaP, InGaAs, and InGaAsP*, 1st ed. (Wiley, 1992).
[20]M. P. Lumb, M. González, J. Abell, K. J. Schmieder, J. G. Tischler, D. A. Scheiman, M. K. Yakes, I. Vurgaftman, J. R. Meyer, and R. J. Walters, "Characterization, modeling and analysis of InAlAsSb Schottky barrier solar cells grown on InP," in *2014 IEEE 40th Photovoltaic Specialist Conference (PVSC)* (IEEE, 2014), pp. 0243–0246.
[21]V. Palankovski and R. Quay, *Analysis and Simulation of Heterostructure Devices*, edited by S. Selberherr, Computational Microelectronics (Springer Vienna, Vienna, 2004).
[22]K. Yang, J. R. East, and G. I. Haddad, "Numerical modeling of abrupt heterojunctions using a thermionic-field emission boundary condition," Solid State Electron. **36**, 321–330 (1993).
[23]O. Breitenstein, J. P. Rakotoniaina, M. H. Al Rifai, and M. Werner, "Shunt types in crystalline silicon solar cells," Prog. Photovolt. Res. Appl. **12**, 529–538 (2004).
[24]H. Kanda, A. Uzum, A. K. Baranwal, T. A. N. Peiris, T. Umeyama, H. Imahori, H. Segawa, T. Miyasaka, and S. Ito, "Analysis of sputtering damage on *I–V* curves for perovskite solar cells and simulation with reversed diode model," J. Phys. Chem. C **120**, 28441–28447 (2016).

08 October 2026 14:11:18

Published under an exclusive license by AIP Publishing